coatings MDPI

Article

Electrochemical Corrosive Behaviors of Fe-Based Amorphous/Nanocrystalline Coating on Stainless Steel Prepared by HVOF-Sprayed

Jifu Zhang [1],*, Chunming Deng [1,2], Jinbing Song [1,3], Changguang Deng [1,3], Min Liu [2] and Mingjiang Dai [1]

[1] Guangdong Institute of New Materials, Guangzhou 510650, China; dengchunming@gdinm.com (C.D.); songjinbing@gdinm.com (J.S.); dengchangguang@gdinm.com (C.D.); daimingjiang@gdinm.com (M.D.)

[2] The Key Laboratory of Guangdong for Modern Surface Engineering Technology, Guangzhou 510650, China; liumin_gz@hotmail.com

[3] National Engineering Laboratory for Modern Materials Surface Engineering Technology, Guangzhou 510650, China

* Correspondence: jfzhang123@163.com; Tel.: +86-20-6108-6656; Fax: +86-20-3723-8531

check for updates

Abstract: In this study, FeCrMnWMoSi amorphous/nanocrystalline coating was prepared on stainless steel by high-velocity oxygen fuel (HVOF) spraying. In order to thoroughly evaluate this novel material, the corrosion behaviors and corrosive film characteristics of the amorphous/nanocrystalline coating in NaCl corrosive media were studied using electrochemical measurement technologies such as potentiodynamic polarization curves and electrochemical impedance spectroscopy (EIS). It was found that the corrosion resistance of Fe-based amorphous/nanocrystalline coating could be attributed to the passive film formed, which consisted of Fe, Cr, Mo, and W oxides. pH has an important influence on the corrosion resistance of amorphous/nanocrystalline coating by changing the pitting corrosion mechanism. Under neutral and acidic conditions, the corrosion mechanism of Fe-based amorphous/nanocrystalline coating was mainly local pitting corrosion. However, under strong alkaline conditions, the amorphous/nanocrystalline coating not only had pitting corrosion, but also had the active dissolution of the passive film. Therefore, the anti-corrosion performance of Fe-based amorphous/nanocrystalline coating under alkaline conditions was not as good as neutral and acidic corrosive medium.

Keywords: amorphous/nanocrystalline coating; electrochemical corrosion; passive film; EIS; corrosion experiments

1. Introduction

With the increase of human activities in the marine environment, many key components (such as ship parts, offshore platforms, oil pipelines, etc.) have had increasingly stringent requirements placed on them regarding the corrosion resistance properties of metal materials, so that these components can meet long life and high reliability design requirements. At present, a number of technologies are utilized to prepare protective coatings on carbon steel for the marine environment, including phosphating, painting, electro- or electroless plating, thermal spraying, diffusion, laser cladding, chemical vapor deposition (CVD), etc. In particular, stainless steels and/or hard chromium plating are frequently used in many fields for their exceptional corrosion resistance. In marine atmospheric environments, however, it appears to be rusted due to a pitting corrosion caused by deposition of airborne sea salts, which is a problem [1,2]. The amorphous alloy has a uniform microstructure; no crystal defects such as grain boundaries and dislocations; and has extremely high strength, toughness, and wear resistance.

Compared with crystalline alloys and stainless steels of the same composition, amorphous alloys have excellent wear and corrosion resistance, so they are ideal coating materials for applications in marine and industrial fields [3,4]. For example, in the power industry, boiler pipes, steam turbine rotating shafts, blades, valve elbows, and other key components are subject to severe wear, corrosion, or erosion, which poses safety hazards to the long-term operation of power station equipment [5]. The application of amorphous coatings to protect the surface of these components is an effective technical method to solve those problems. Amorphous coatings also have huge application prospects for protection of steel facilities (such as television towers, bridges, road facilities, floodgates, microwave towers, high-voltage transmission towers, underground cable supports, and even transportation and underground storage of nuclear waste) from long-term exposure to harsh outdoor environments [6]. Among those amorphous alloy materials, Fe-based amorphous alloys are the most attractive due to their unique properties including high hardness, superior corrosion and wear resistance, and relatively low cost [7–9]. They can be successfully coated on steel substrate by thermal spray technology [10–14], where the amorphous structure is retained due to sufficiently rapid cooling that prevents long-range diffusion and crystallization. These advantages have demonstrated an enhanced comprehensive performance on steel surfaces in industrial applications, such as a better corrosion resistance than electroplated Cr and stainless steel in NaCl solution [15,16].

Many scholars have researched the corrosion behavior of amorphous coatings [17–26]. For example, M.S. Bakare et al. studied the corrosion behavior of both crystalline and largely amorphous forms of $Fe_{43}Cr_{16}Mo_{16}C_{15}B_{10}$ alloy in 0.5 M H_2SO_4 and 3.5% NaCl electrolytes; it was found that the improved corrosion behavior of the largely amorphous material could be attributed to its homogeneity, and particularly to the elimination of the Mo-rich phase that underwent preferential corrosion in the crystalline form of the material [17]. Masaaki Naka et al. studied the amorphous Fe-Cr-P-C and Fe-Cr-Ni-P-C alloys by total immersion tests and electrochemical methods in acidic and neutral solutions containing chloride and indicated that the amorphous Fe-base alloys did not suffer pitting corrosion; they considered that the high corrosion resistance of the amorphous iron alloys resulted partly from the presence of chromium and large amounts of phosphorus and partly from a homogeneous single phase amorphous structure [19]. Zhang et al. studied the corrosion resistance of $Fe_{48}Cr_{15}Mo_{14}C_{15}B_6Y_2$ amorphous coating in NaCl solution. The results of electrochemical measurement show that the coatings exhibited extremely wide passive region and relatively low passive current density in acidic NaCl solutions, which illustrates their superior ability to resist localized corrosion [23].

Since Fe-based amorphous/nanocrystalline coating exhibits excellent corrosion resistance, it is required to test its corrosion behavior in different pH corrosive medium solutions (especially under strong acid and strong alkaline conditions) in order to broaden its application range. At the same time, recognition of the composition and characteristic evolution of the passive film formed on Fe-based amorphous/nanocrystalline coating after long-term immersion in corrosive medium are also helpful to understand the corrosion protection and failure mechanism of the coating.

2. Experimental Procedure

2.1. Specimen Preparation

304 stainless steel with dimensions of 50 mm × 50 mm × 8 mm were selected as substrate. Prior to thermal spraying, the substrates were ultrasonically cleaned in ethanol, and then grit-blasted to achieve a roughened surface. FeCrMnWMoSi (Cr 18.2, Mo 12.6, Mn 1.5, W 6.4, B 2.4, C 0.9, Si 0.9, and Fe balance, in mass %) amorphous powder with particle size of 15–45 μm was chosen as thermal spray powder. A high-velocity oxygen fuel (HVOF) thermal spraying gun (GTV K_2 system) was utilized to deposit Fe-based amorphous/nanocrystalline coatings onto the steel substrate. Optimum spraying parameters were taken to deposit the coatings with uniform distribution and thickness as described in Table 1.

Table 1. Spray parameters for deposition of Fe-based amorphous/nanocrystalline coatings.

Parameters	Optimized Value
Oxygen (O_2) (L/min)	900
Kerosene (Ke) (L/h)	22
O_2/Ke burning ratio(λ)	1.18
Combustion pressure (Bar)	8.5
Nozzle	150/11
Carrier gas (N_2) (L/min)	9
Powder feed rate (g/min)	100
Spray distance (mm)	380
Transverse speed (mm/s)	1000
Deposition efficiency (%)	30–45

In the process of spraying, the substrate temperature was controlled by compressed air and the deposited coatings were about 0.3 mm in thickness. After spraying process, small square samples were cut by using wire electrical discharge machining (WEDM) to make samples for electrochemical corrosion testing and microscopic analysis. The samples for electrochemical corrosion testing were polished to surface roughness of $R_a = 0.1$ μm using a diamond abrasive paper, while samples for microscopic analysis were ground to a cutting edge of more than 1 mm to avoid the heat-affected zone reduced by the WEDM on the microstructure of the coating. Vacuum heat treatment was carried out at 650 °C for 4 h and 800 °C for 4 h to explore the thermodynamic stability and crystallization temperature of the Fe-based amorphous/nanocrystalline coating, respectively. For comparison, Cr plating was electrodeposited in 180 g/L CrO_3 + 1.8 g/L H_2SO_4 solution at 55–60 °C with a cathode current density (D_k) = 30 A/dm^2. The thickness of as-deposited Cr plating was about 0.1 mm.

2.2. Test Methods

The microscopic morphologies were characterized by scanning electron microscopy (SEM, JEOLJXA-8100, JEOL, Akishima, Japan) The phase composition of the coatings was identified by X-ray diffractometer (XRD, Philips X'PertPro, PANalytical B.V., Ndehofen, The Netherlands) with a Cu Kα source. The surface analyses of passive film were conducted by X-ray photoelectron spectroscopy (XPS, ESCALAB 250, VG Company, UK) with a Mg Kα source. In order to remove the contaminants on the surface of the sample and obtain the elemental distribution of the passive film profile, the surface of the sample was etched by argon ion sputtering, and the correspondence between the sputtering depth and time was 0.1 nm/s.

The electrochemical measurements were performed using a Princeton Applied Research (PAR, PARSTAT4000A, Advanced Measurement Technology, Inc., Oak Ridge, TN, USA) electrochemical workstation with VersaStudio test software v2.4. Specimens with exposure area of 1.77 cm^2 were used as working electrodes, platinum sheet was used as counter electrode, and saturated calomel electrode (SCE) was used as reference electrode. The corrosive medium for electrochemical measurement based on 3.5 wt % NaCl solution. The pH of the NaCl solution was adjusted by HCl and NaOH, and three solutions with pH = 1, pH = 7, and pH = 13 were respectively obtained to simulate the corrosive medium of strong acid (pH = 1), strong alkali (pH = 13) and neutral (pH = 7) conditions. All electrochemical measurements were carried out at room temperature. Potentiodynamic polarization curves were obtained at the scan rate of 0.5 mV/s, and samples were immersed for 30 min before testing. EIS was used to test the corrosion behavior of samples during long-term immersion. The signal amplitude of EIS was 10 mV and the frequency ranged was between 1×10^5 and 1×10^{-2} Hz. Cview software and Zsimpwin software v3.20 were used to fit and analyze polarization curves and EIS curves, respectively. All of our tests tested more than three samples to ensure reproducibility of the test results.

3. Results and Discussion

3.1. Phase Structure of Fe-Based Amorphous/Nanocrystalline Coating (AC)

Figure 1 shows an XRD diffraction pattern of Fe-based amorphous powder and coating deposited by HVOF. It can be seen that there was no substantial Bragg diffraction peak (crystal peak) but a very low diffusion peak appeared at $2\theta = 44°$ (Figure 1a), indicating the amorphization degree of FeCrMnWMoSi powder was very high. The diffusion peak intensity of the amorphous/nanocrystalline coating deposited by HVOF was significantly enhanced compared to the amorphous powder, but there was still no crystallization peak phenomenon (Figure 1b). Previous research [24] shows that the microstructure of the HVOF-deposited coating was amorphous + nanocrystalline, so the diffusion peak at $2\theta = 44°$ was the diffraction from the nanocrystalline in the coating. Moreover, the XRD diffraction spectrum of the coating after heat treatment at 650 °C was still a diffuse peak, which means that the crystallization or nanocrystalline growth of the amorphous coating was not significant (Figure 1c). However, the crystallization of the amorphous coating occurred at 800 °C since the Bragg diffraction peaks that appeared in the XRD diffraction pattern were very obvious (Figure 1d). The phase structure of the diffraction pattern in Figure 1d can be determined by Jade software. It was confirmed that the crystalline phase was mainly composed of Fe-Cr solid solution, whose diffraction peaks appear in $2\theta = 44.2°$, $64.52°$ and $81.5°$, in addition, the crystal phase of Fe-Mo, Fe-Si and Cr-Si phases also appeared.
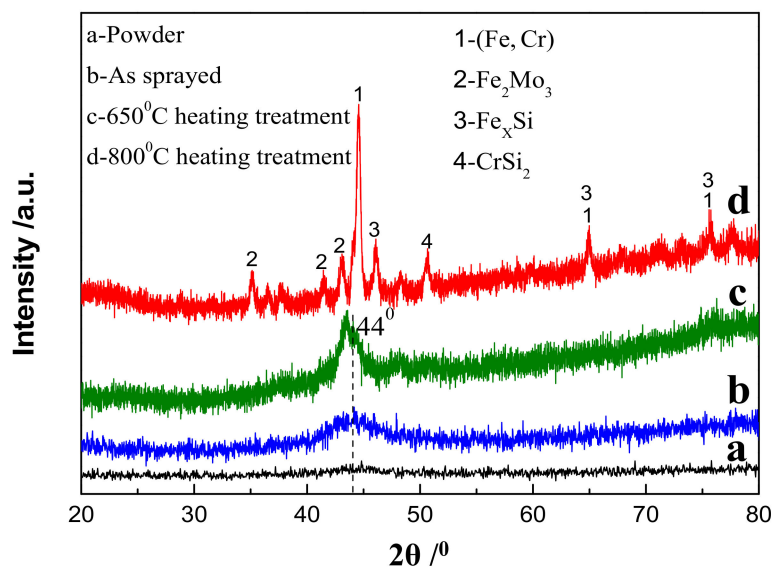

Figure 1. X-ray diffractometer (XRD) spectrum of (**a**) FeCrMnWMoSi amorphous powder, (**b**) as-sprayed coating, and coating specimens by heat treatment at (**c**) 650 °C for 4 h and (**d**) 800 °C for 4 h.

The above analysis indicates that HVOF spraying was an effective method for preparing amorphous/nanocrystalline coating, which can nearly maintain the original amorphous structure of the powder, and the sprayed Fe-base amorphous/nanocrystalline coating can service within 650 °C without changes in phase structure.

3.2. Corrosion Resistance of Fe-Based Amorphous/Nanocrystalline Coating (AC) vs. Conventional Materials

Figure 2 shows the comparison of polarization curves between Fe-based amorphous/nanocrystalline coatings and conventional corrosion resistant materials in 3.5 wt % NaCl solution at pH = 7. It can be seen that all three materials—304 stainless steel, Cr plating, and Fe-based amorphous/nanocrystalline coating—exhibited passivation behavior. That is, the current density did not increase with increase of potential during anodic polarization, but was maintained at a relatively stable value (passivation current density, I_p), implying passive film can form on those metals, which will inhibit the further

dissolution of the metal electrode surface. However, the anti-corrosion characteristics of the passive film formed on various metals' surface and various solutions were different. The corrosion behavior of the passive film will usually start at local pitting corrosion when the anode polarization potential exceeds a certain value (pitting potential, E_{pit}). As a result, the passive film begins to break down and dissolve, causing the current density to increase sharply. Generally, pitting potential (E_{pit}), passivation interval ($E_{pit} - E_{corr}$), and passivation current densities (I_p) are used to evaluate the pitting corrosion resistance of passive metals. The characteristic parameters of those materials in 3.5 wt % NaCl solutions tested by polarization curves are listed in Table 2.
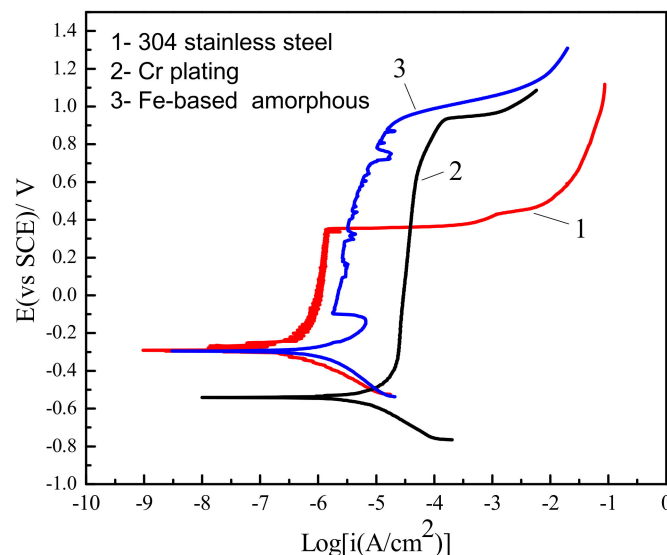

Figure 2. Comparison of polarization curves between Fe-based amorphous/nanocrystalline coatings and conventional corrosion-resistant materials in 3.5 wt % NaCl solution at pH = 7.

Table 2. Corrosion parameters of different materials by the polarization curves fitting.

Samples	E_{pit} (mV$_{SCE}$)	E_{corr} (mV$_{SCE}$)	$E_{pit} - E_{corr}$ (mV)	I_p (A/cm^2)
304 stainless steel	388 ± 11	−277 ± 11	665 ± 20	$(0.73–1.3) \times 10^{-6}$
Cr plating	918 ± 20	−543 ± 12	1461 ± 34	$(0.20–1.5) \times 10^{-4}$
Fe-based AC	929 ± 18	−294 ± 17	1223 ± 34	$(0.22–1.1) \times 10^{-5}$

Table 2 shows that the passive film on 304 stainless steel had the lowest I_p to $(0.73–1.3) \times 10^{-6}$ A/cm^2, but the passive film was also the most unstable with the ($E_{pit} - E_{corr}$) only 627 mV. The I_p of Cr plating was much higher than that of the 304 stainless steel, but the ($E_{pit} - E_{corr}$) was increased a lot to 1461 mV. In contrast, the ($E_{pit} - E_{corr}$) of the Fe-base amorphous/nanocrystalline coating was close to that of Cr plating, while its I_p was also maintained at a relatively low level to $(0.22–1.1) \times 10^{-5}$ A/cm^2, meaning that a complete passive film covered the electrode, then when the anode potential was polarized to 929 mV$_{SCE}$, the pitting corrosion of the passive film occurred.

Figure 3 shows the surface morphology of various samples after polarization curve test. It can be seen that the corrosion appearance of 304 stainless steel was very prominent with many deep corrosion holes on the surface (Figure 3a). Usually, the corrosion morphology caused by grain boundary galvanic corrosion may cause severe corrosion voids or corrosion cracks. Therefore, it was confirmed the holes will be generated by grain boundaries of 304 stainless steel [27]. In contrast, Cr plating was intact after anodization, but there were many micro-cracks on the specimen after magnifying observation (Figure 3b). Those micro-cracks were inevitable microscopic defects formed during the electroplating of Cr, which obviously cannot effectively block the invasion of corrosive media, and is also not conducive to formation of a complete passive film on the electrode; as a

result, the I_p of the Cr plating layer was the largest. As for Fe-based amorphous/nanocrystalline coating, porosity was considered to be an important and inevitable property of thermally sprayed coatings, which considerably influences the corrosion resistance of the coating [26]. Simultaneously, multiple phases exist in Fe-based amorphous/nanocrystalline coating, so local galvanic corrosion resulting from grain boundary corrosion may occur. However, the surface morphology of Fe-based amorphous/nanocrystalline coating did not show any obvious corrosion holes or corrosion cracks; it was similar to its morphology before the testing (Figure 3c). Therefore, it can be deduced that the amorphous/nanocrystalline structure [24] of Fe-based coating makes chemical inhomogeneity and microscopic defects less probable; this can effectively reduce the possibility of localized galvanic corrosion. Therefore, the Fe-based amorphous/nanocrystalline coating exhibited better resistance to localized corrosion in NaCl solution than 304 stainless steel and Cr plating.
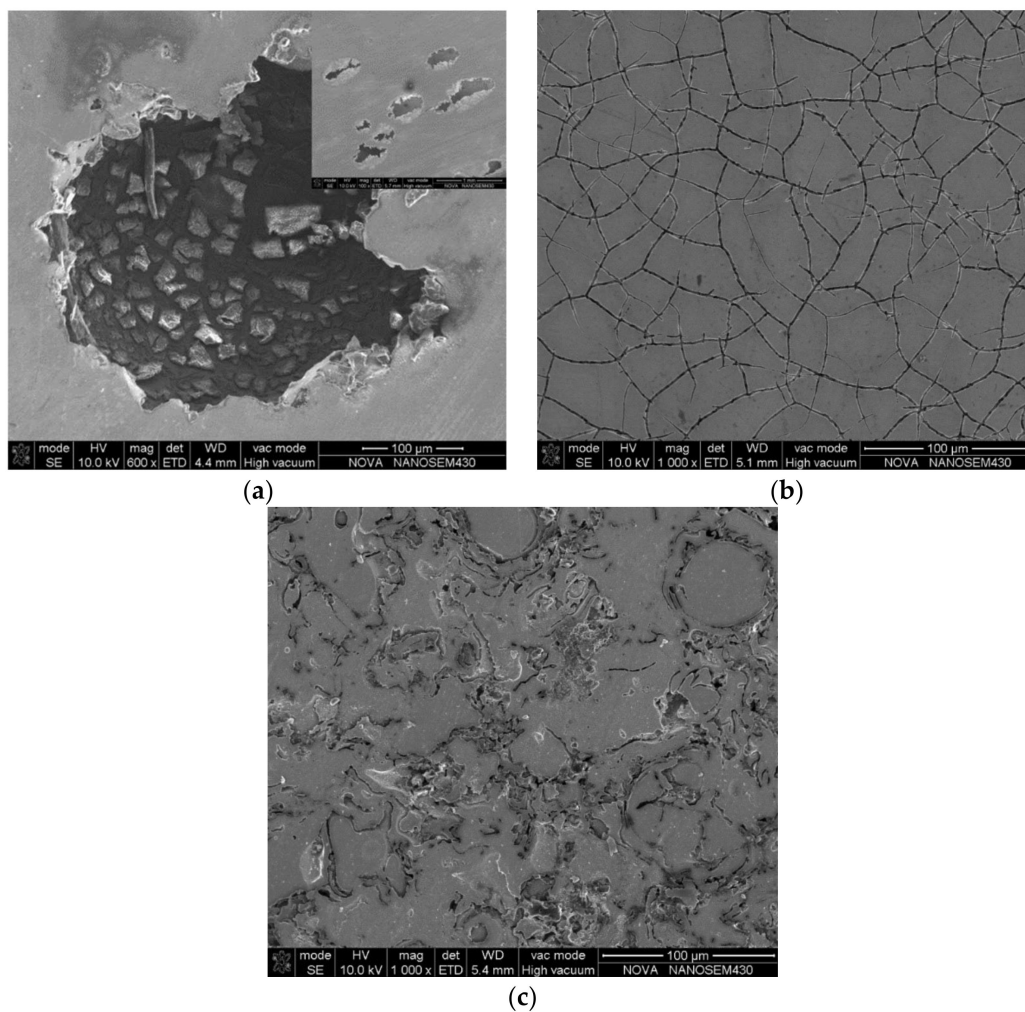

(**a**)

(**b**)

(**c**)

Figure 3. Surface morphology of various samples after polarization curves test at pH = 7: (**a**) 304 stainless steel; (**b**) Cr plating; (**c**) amorphous/nanocrystalline coating.

3.3. The Effects of pH Values on Corrosive Behaviors of Fe-Based Amorphous/Nanocrystalline Coating

For further research into the corrosion behavior of Fe-based amorphous/nanocrystalline coating, the coating was subjected to corrosive media of strong acid (pH = 1), strong alkali (pH = 13) and neutral (pH = 7) conditions. Figure 4 showed that corrosive media with different pH values had an important influence on the electrochemical polarization behavior of Fe-based amorphous/nanocrystalline coating. When polarized under a strongly acidic (pH = 1) NaCl solution, passive film can also form on Fe-based amorphous/nanocrystalline coating, but the chemical stability of the passive film was obviously worse

than that formed in the neutral solution, since the I_p was higher at $(1.91–8.2) \times 10^{-5}$ A/cm^2 and $(E_{pit} - E_{corr})$ was shorter at 778 mV. When polarized under a strong alkaline (pH = 13) NaCl solution, the corrosion potential (E_{corr}) of Fe-based amorphous/nanocrystalline coating raised from about -294 mV$_{SCE}$ in neutral conditions to 588 mV$_{SCE}$, but the $(E_{pit} - E_{corr})$ was significantly shortened, and the I_p $(1.34–1.5 \times 10^{-2}$ A/cm$^2)$ increased by almost four orders of magnitude compared to that tested in neutral solution. The above phenomenon indicates that the chemical stability of passive film formed under strong acidic conditions was much less stable than that formed under neutral conditions, and that it is difficult to form a complete or stable passive film on the coating under strongly alkaline conditions, resulting in a decrease in corrosion resistance of the amorphous/nanocrystalline coating. It can be also deduced that the formation of passive film caused the E_{corr} of the coating to decline.
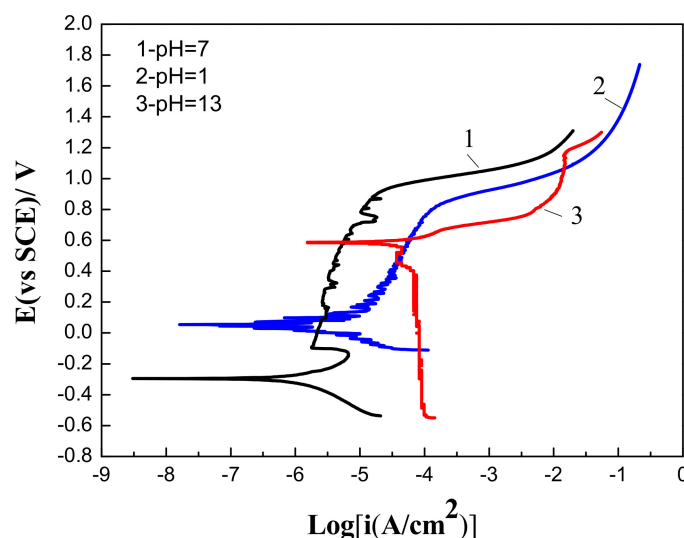

Figure 4. Polarization curves of Fe-based amorphous/nanocrystalline coatings in 3.5 wt % NaCl solution at different pH values.

Table 2 shows that the passive film on 304 stainless steel had the lowest I_p, $(0.73–1.3) \times 10^{-6}$ A/cm^2, but the passive film was also the most unstable with the $(E_{pit} - E_{corr})$ only 627 mV. The I_p of Cr plating was much higher than that of the 304 stainless steel, but the $(E_{pit} - E_{corr})$ was increased significantly to 1461 mV. In contrast, the $(E_{pit} - E_{corr})$ of the Fe-based amorphous/nanocrystalline coating was close to that of Cr plating, while its I_p was also maintained at a relatively low level to $(0.22–1.1) \times 10^{-5}$ A/cm^2, meaning that a complete passive film covered on the electrode, then when the anode potential was polarized to 929 mV$_{SCE}$, the pitting corrosion of the passive film occurred.

The evolution of corrosion characteristics of Fe-based amorphous/nanocrystalline coating in various pH NaCl solutions was monitored by EIS as shown in Figure 5. Figure 5a shows that in neutral NaCl solution (pH = 7), the Nyquist plots are characterized by two capacitive semicircles in the high frequency (HF) and low frequency region (LF), corresponding to two response peaks which appeared in the Bode plots in Figure 5b. Usually, if there is an ideal passive film with uniform thickness formed on the metal, only the growth and dissolution process of the passive film is performed on the electrode; in that case, the thickness of the passive film becomes the only state variable that affects the Faraday current density, so the EIS will display only one time constant [28]. However, in the NaCl solution, Cl$^-$ will have a corrosion effect on the passive film by causing pitting corrosion, resulting in formation of many small micro-holes on the passive film, so the state variables affecting the Faraday current density include the two time constants of passive film thickness and Cl$^-$ corrosion, which correspond to the HF and LF capacitive semicircles response in the EIS plots, respectively. In strongly acidic NaCl solution (pH = 1), the radius of the HF capacitive semicircles become larger and larger (Figure 5c) with increasing immersion time while the radii of LF capacitive semicircles gradually become smaller, or even disappear. However, the response curve of the impedance spectrum can still be regarded as

the existence of two time constants in HF region and LF region, respectively. In strongly alkaline NaCl solution (pH = 13), it can be observed from the Nyquist diagram in Figure 5e that the radius of both the HF and LF capacitive semicircles become smaller with increasing immersion time, while the number of response phase peaks in Bode plots (Figure 5f) gradually transition from two to three, implying the time constant of this electrode system in alkaline solution was changed from two to three.
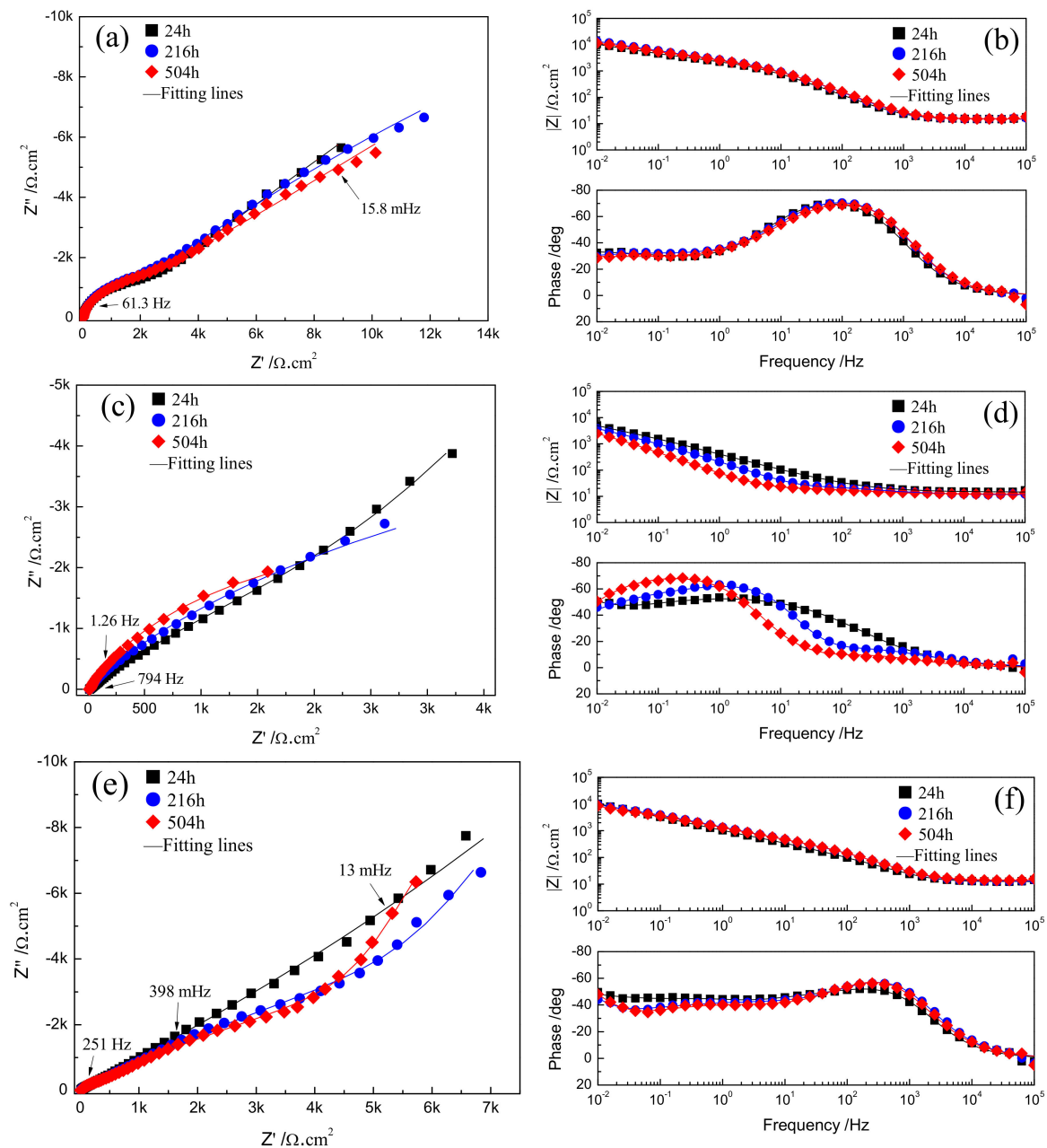

Figure 5. EIS plots and fitting results of Fe-based amorphous/nanocrystalline coatings in 3.5% NaCl solution at different pH for long time immersion: (**a,b**) Neutral solution (pH = 7); (**c,d**) strong acid solution (pH = 1); (**e,f**) strong alkaline (pH = 13) solutions.

It is considered that the corrosion mechanism of Fe-based amorphous/nanocrystalline coating in strong acid solution is as same as that in the neutral solution; that is to say, only a single pitting corrosion of the passive film occurs, so the typical equivalent circuit diagram of pitting corrosion of passive film on metal surface [29,30] in Figure 6a can be used to fit the experimental data of EIS in neutral solution (pH = 7) and strong acid solution (pH = 1). R_{sol} represents the electrolytic resistance;

the constant phase component of CPE_{film} represents the capacitance characteristics of passive film on amorphous/nanocrystalline coating; while R_{pore}, R_p, and CPE_{dl} represent the in-hole resistance, polarization resistance and interfacial capacitance in the corrosion spots of passive film, respectively. The time constant corresponding to the HF region contributes to the response of passive film capacitance (CPE_{film}) and the in-hole resistance (R_{pore}), while the time constant corresponding to the LF region contributes to the response of the electric layer capacitance (CPE_{dl}) and the polarization resistance (R_p) of the corrosion in the hole. The fitting parameters were listed in Table 3 and the fitting curves were drawn in Figure 5a–d by real lines; it can be seen that the model results are also significantly close to the experimental data.
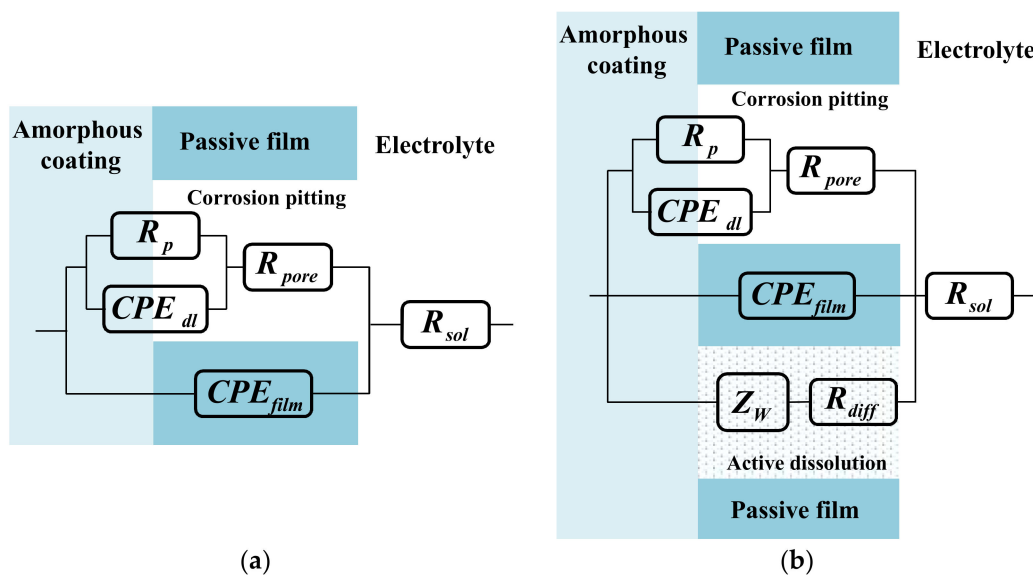

(a)　　　　　　　　　　　　　　　　　　　　　　　　　(b)

Figure 6. Equivalent circuits proposed for fitting of EIS plots in Figure 5 according to various pH of NaCl solution: (**a**) Model for single corrosion mechanism of pitting corrosion; (**b**) model for double corrosion mechanism of pitting corrosion and chemically active dissolution.
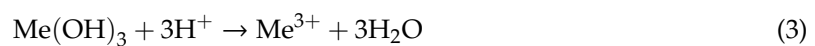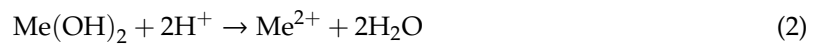
Table 3. The fitting parameters of EIS in neutral NaCl and acidic NaCl solution by the proposed equivalent circuit (EC) in Figure 6a.

Samples	R_{sol} (cm^2)	R_{pore} (cm^2)	R_p (cm^2)	CPE_{film}		CPE_{dl}	
				Y_0 (cm$^{-2}\cdot$s^{-n})	n	Y_0 (cm$^{-2}\cdot$s^{-n})	n
pH = 7, 24 h	14.91	1561	1.7×10^5	2.77×10^{-5}	0.89	3.39×10^{-4}	0.44
pH = 7, 216 h	14.96	1060	3.7×10^{11}	1.84×10^{-5}	0.91	2.24×10^{-4}	0.38
pH = 7, 504 h	15.31	831.4	1.7×10^6	1.82×10^{-5}	0.90	2.36×10^{-4}	0.35
pH = 1, 24 h	14.55	10530	4.6×10^4	7.8×10^{-4}	0.62	13.7×10^{-4}	1
pH = 1, 216 h	11.45	18	1.5×10^4	10.3×10^{-4}	0.59	3.5×10^{-4}	0.96
pH = 1, 504 h	12.17	9	6.6×10^3	9.4×10^{-4}	0.68	21.6×10^{-4}	0.87

The fitting parameters by the proposed equivalent circuit (EC) are listed in Table 3 and the fitting curves are drawn in Figure 5a–d by real lines; it can be seen that the model results are significantly close to the experimental data. The electrochemical parameters in the corrosion spots are an important basis for the degree of pitting corrosion. Since the polarization resistance (R_p) directly reflects the resistance of the electrochemical reaction occurring in the micro-holes, its value can be used to express the corrosion rate of pitting. The larger the R_p value, the greater the resistance of pitting corrosion, that is, the lower the corrosion rate of pitting corrosion. Conversely, the smaller the R_p value, the higher the corrosion rate of pitting corrosion. By comparing the R_p values in Table 3, it can be seen that R_p drops by at least an order of magnitude when compared at different immersion times when the pH of corrosive medium

solution is adjusted from neutral to strongly acidic, which means the high concentration of H^+ in the acidic medium accelerates the pitting corrosion of passive film on amorphous/nanocrystalline coating.

The usual pitting theory holds that once the pore corrosion occurs, the pH of the solution in the pore will be significantly lower than that of the bulk solution outside the pore, so the propagation of pitting corrosion itself is carried out under an acidic condition. However, when the concentration of H^+ in the solution outside the pore is higher, it will diffuse into the pore and accelerate the dissolution of precipitate in the pore as in Equations (1)–(3) [29,31]:

$$MeOH + H^+ \rightarrow Me^+ + H_2O \tag{1}$$

$$Me(OH)_2 + 2H^+ \rightarrow Me^{2+} + 2H_2O \tag{2}$$

$$Me(OH)_3 + 3H^+ \rightarrow Me^{3+} + 3H_2O \tag{3}$$

The above reaction is synergistic with the destruction of Cl^-, thereby accelerating the occurrence and expansion of small pore corrosion. The dissolution of the precipitate causes the increase of ionic conductivity in the pitting. After long-term immersion, the metal oxide in the small pores are dissolved under acidic conditions, resulting in the reduction of the R_{pore} by about two orders of magnitude. R_p is significantly lower than that in neutral solution. The above results lead to the conclusion that the corrosion mechanism of Fe-based amorphous/nanocrystalline coating in acid solution is mainly the effect of H^+ accelerating the pitting corrosion rate of the passive film.

It is conceivable that the destruction of passive film on Fe-based amorphous/nanocrystalline coating in alkali solution was much more complex than that in neutral and acidic solution. The radius of LF capacitive semicircles gradually becomes smaller, indicating that pitting corrosion of amorphous/nanocrystalline coating is suppressed but still exists. However, it is much more noteworthy that the Nyquist diagram exhibits the impedance as a straight slope line in the LF region, which corresponds to the impedance of Warburg line. It is generally believed that the appearance of the Warburg line is due to the presence of Faraday impedance controlled by the diffusion step on the electrode surface. It was supposed that the amorphous/nanocrystalline coating chemically reacts with the strong alkali solution, resulting in the continuous diffusion of the reaction products from the electrode surface into the solution body to form a certain diffusion layer. Therefore, the corrosion mechanism of amorphous/nanocrystalline coating under alkaline solution has changed significantly from a single pitting corrosion to a double corrosion mechanism of pitting corrosion and chemically active dissolution. The schematic diagram and proposed equivalent circuit (EC) model in Figure 6b can vividly illustrate the double corrosion mechanism of pitting corrosion and chemically active dissolution, where R_{sol}, CPE_{film}, R_{pore}, R_p, and CPE_{dl} still represent the electrolytic resistance, passive film capacitance, in-hole resistance, pitting polarization resistance, and interfacial capacitance, respectively. The only difference is that Warburg impedance of Z_w and resistance of R_{diff} are adopted to simulate the impedance characteristic of the active dissolution zone of amorphous/nanocrystalline coating. The fitting parameters by the proposed EC are listed in Table 4 and the fitting curves are drawn in Figure 5e–f by real lines; it can be seen that the model results are also significantly close to the experimental data.

Table 4. The fitting parameters of EIS in alkaline NaCl solution by the proposed EC in Figure 6b.

Samples	R_{sol} (cm²)	R_{pore} (cm²)	R_p (cm²)	R_{diff} (cm²)	CPE_{film} Y_0 (cm⁻²·s⁻ⁿ)	n	CPE_{dl} Y_0 (cm⁻²·s⁻ⁿ)	n	$Z_w - Y_0$ (cm²·s⁻¹/²)
pH = 13, 24 h	12.44	6	8.7×10^{14}	1118	6.50×10^{-6}	0.99	2.61×10^{-4}	0.52	1.4×10^{-4}
pH = 13, 216 h	12.73	20380	1.4×10^{13}	205.8	1.89×10^{-5}	0.88	8.10×10^{-4}	1.00	2.7×10^{-4}
pH = 13, 504 h	13.89	14560	8.3×10^{13}	242.5	2.00×10^{-5}	0.88	9.24×10^{-4}	1.00	2.9×10^{-4}

The fitting values of R_p and R_{pore} in Table 1 rise sharply after long-term immersion in strong alkaline NaCl solution, compared to those in neutral and acidic solutions, which further indicates that the pitting corrosion of passive film is greatly suppressed. Instead, the corrosion mechanism of the Fe-based amorphous/nanocrystalline coating is chemically dissolved with a relatively low R_{diff}.

Under alkaline conditions, the corrosion dissolution of the passive film on amorphous/nanocrystalline coating can be explained by the reaction of an amphoteric metal of Cr with the alkaline as in Equation (4) [32,33]:

$$Cr(OH)_3 + 5OH^- \rightarrow CrO_4^{2-} + 4H_2O + 3e \tag{4}$$
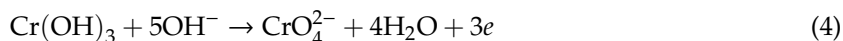
The above reaction causes many intact passive films to suffer dissolution. On the other hand, OH^- will also have a synergistic effect with the Cl^- on the destruction of the passive film as described in Equations (5) and (6) [34,35].

$$MeOH + Cl^- \rightarrow MeOHCl + e \tag{5}$$

$$MeOHCl + Cl^- \rightarrow MeOHCl_2 + e \tag{6}$$
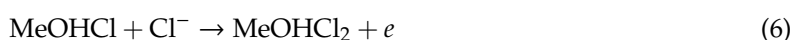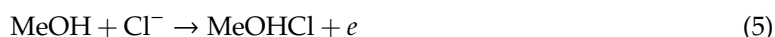
The adsorbed Cl^- changes the composition and properties of the passive film at the adsorption site and makes the ionic conductivity and dissolution rate of the passive film much larger than that of sites without Cl^- adsorption, resulting in local active point and dissolution of the passive film, which is the "pitting corrosion". It's worth noting that the adsorbed Cl^- does not cover the electrode surface homogeneously, but preferentially adsorbs on some points where chemical inhomogeneity or physical defects exist, such as grain boundaries, micro-cracks, impurity segregation, etc. Meanwhile, the adsorbed Cl^- will compete with the surrounding O elements to capture metal cations; finally, the combination forms a soluble chloride, which causes damage to the metal material [36].

Malik et al. [31] observed that the repassivating potential of AISI 316L in strongly acidic NaCl solution appears at a much higher positive potential than at neutral NaCl solution under similar conditions of temperature and $[Cl^-]$, while no repassivating potential was observed in strong alkali NaCl solution. This leads to the conclusion that pitting corrosion of passive film has the opportunity of repassivation under strong acidic and neutral conditions, while pitting corrosion is an irreversible process under strong alkaline conditions. This also means that in the strong alkali solution, the surface the Fe-based amorphous/nanocrystalline coating is chemically active, resulting in much more severe chemical dissolution than pitting corrosion; this mechanism essentially the reason why Fe-based amorphous/nanocrystalline coating has poor resistance to alkaline solution corrosion.

3.4. Composition Analysis of Passive Film Formed on Fe-Based Amorphous/Nanocrystalline Coating

The FeCrMnWMoSi amorphous/nanocrystalline coating was immersed in 3.5% NaCl solution at various pH for 24 h to form a complete passive film on the coating, and then the elemental composition and chemical state of the passive film was investigated by XPS analysis. In the XPS analysis process, the surface of the sample was sputtered with argon ions for different times to achieve different thickness stripping of the passive film to obtain the element profile distribution. Since the XPS results showed that the passive film composition formed on the coating was almost similar, we only exhibited the XPS test results of sample in neutral NaCl solution as shown in Figure 7.

Comparing the binding energy of each element in the test result with the standard spectrum database of XPS [37], it can be determined that the main constituent elements of the passive film is Fe, Cr, W, Mo, and O. It was found that the Mn, B, and Si elements in the coating did not participate in the formation of passive film. A narrow-area scan of the constituent elements (Fe, Cr, Mo, and W) in the passive film yielded the accurate peak position of the elements as shown in Figure 8. It confirmed that the characteristic peaks of Fe $2p_{3/2}$ appeared at 709.1 and 710.9 eV in the binding energy spectrum, corresponding to the characteristic peaks of Fe_3O_4 and Fe_2O_3, respectively. The characteristic peaks of Cr $2p_{3/2}$ appeared at 576.1 and 577.6 eV, corresponding to the characteristic peaks of Cr_2O_3 and $Cr(OH)_3$, respectively. The characteristic peaks of Mo $3d_{5/2}$ appeared at 229.7 and 232.9 eV corresponding to the

characteristic peaks of MoO_2 and MoO_3, respectively. Moreover, the characteristic peaks of W $4f_{7/2}$ appeared at 32.8 and 35.0 eV, corresponding to the characteristic peaks of WO_2 and WO_3, respectively.
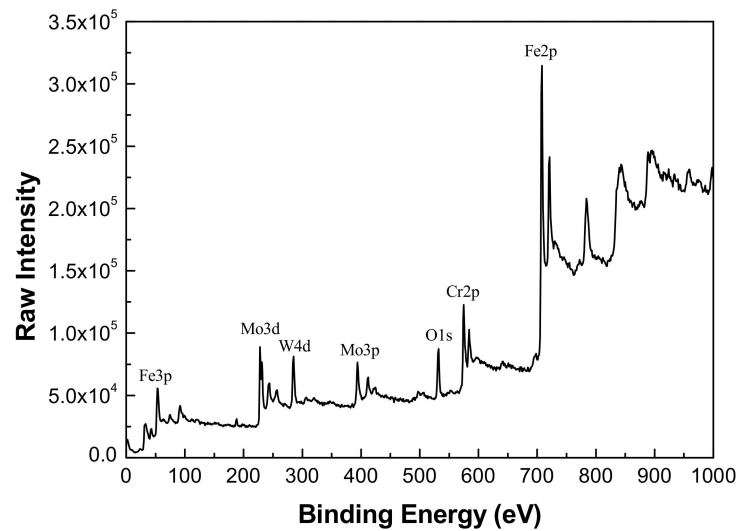
Figure 7. X-ray photoelectron spectroscopy (XPS) spectra for Fe-based amorphous/nanocrystalline coating after argon ion sputtering for 10 s.
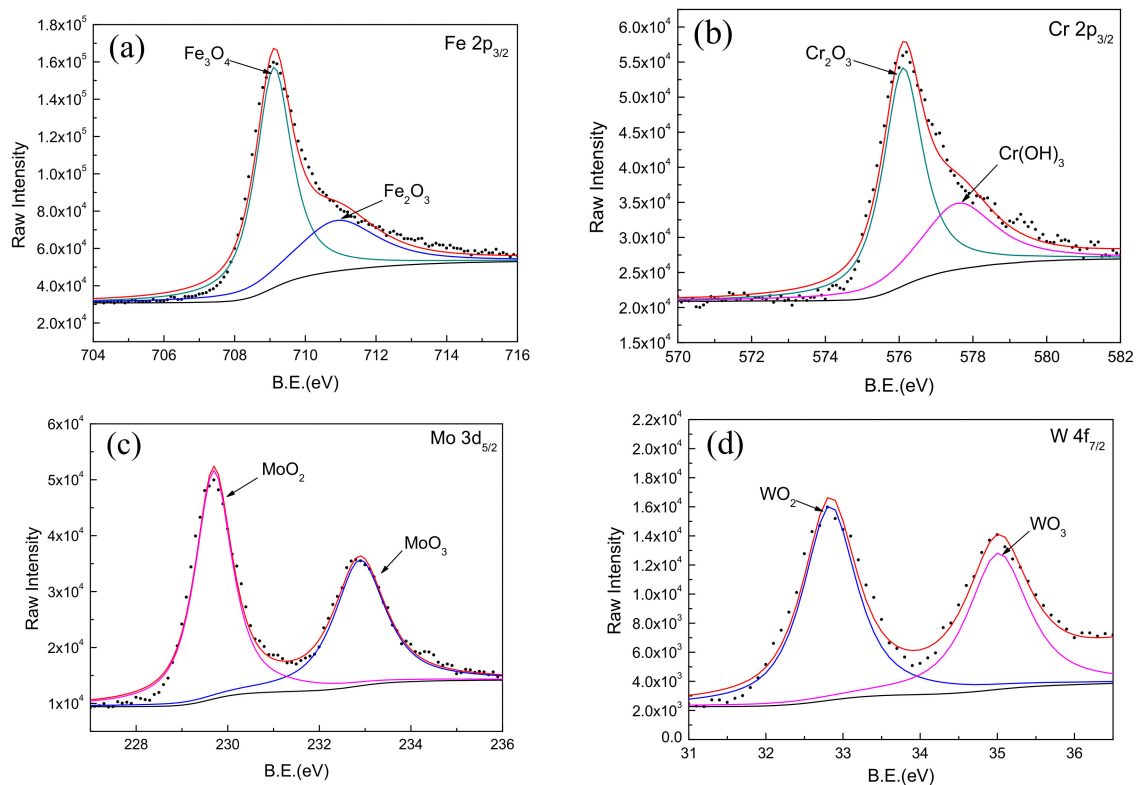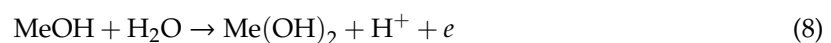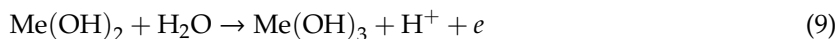
Figure 8. XPS spectra for Fe, Cr, Mo, and W elements in passive film on Fe-based amorphous/ nanocrystalline coating. (**a**) Fe $2p_{3/2}$; (**b**) Cr $2p_{3/2}$; (**c**) Mo $3d_{3/2}$; (**d**) W $4f_{7/2}$;

Generally, the hydrolysis and oxidation of metal (Me = Fe, Cr) elements can be deduced as per Equations (7)–(10) [38]:

$$Me + H_2O \rightarrow MeOH + H^+ + e \qquad (7)$$

$$MeOH + H_2O \rightarrow Me(OH)_2 + H^+ + e \qquad (8)$$

$$Me(OH)_2 + H_2O \rightarrow Me(OH)_3 + H^+ + e \tag{9}$$

$$2Me(OH)_3 \rightarrow Me_2O_3 + 3H_2O \tag{10}$$

It is worth noting that the addition of Mo and W in the coating not only helps to improve the amorphous state of the Fe-based coating, but also participates in the formation of passive film on the coating; this is consistent with the phenomenon observed by previous researchers [39]. It was confirmed that the enrichment of Mo in the amorphous coating promotes the enrichment of Cr_2O_3 as shown in Figure 8b. The Cr_2O_3 with cation vacancies behaved as p-type semiconductor in passive film [40]. Comparing with $Cr(OH)_3$, Cr_2O_3 had lower point defect concentration (i.e., cation vacancies) [41]. Therefore, more Cr_2O_3 in passive film could significantly improve the corrosion resistance of Fe-based amorphous/nanocrystalline coating in NaCl solution. On the other hand, it was considered that the presence of Mo in passive film will reduce the number and the sizes of both nucleations and metastable pits, so reduces the probability of generating stable pits [42–45]. Furthermore, the addition of tungsten is effective in improving the corrosion resistance of amorphous iron alloys, though tungsten is less effective than Cr and Mo. Naka et al. [19] observed that with an increase in the tungsten content in the Fe–W alloy, the corrosion potential was raised. The Fe–W alloys with tungsten of 6 wt % or more was passivated and the passivation current density decreased with the increase in the tungsten content. These results show that the addition of tungsten is effective in improving the corrosion resistance of amorphous iron alloy.

4. Conclusions

HVOF spraying was an effective method for preparing Fe-based amorphous/nanocrystalline coating, which can maintain the original amorphous structure of the powder, and the sprayed Fe-based amorphous/nanocrystalline coating can service within 650 °C without changes in phase structure.

The Fe-based amorphous/nanocrystalline coating exhibited better resistance to Cl^- pitting in NaCl solution than 304 stainless steel and Cr plating. pH has an important influence on the corrosion behavior of Fe-based amorphous/nanocrystalline coating. Under neutral and acidic conditions, the corrosion mechanism of Fe-based amorphous/nanocrystalline coating was mainly local pitting corrosion, while under strong alkaline conditions, the amorphous/nanocrystalline coating not only had pitting corrosion, but also had the active chemical dissolution of the passive film. Therefore, the anti-corrosion performance of Fe-based amorphous/nanocrystalline coating under alkaline conditions was not as good as neutral and acidic corrosive media.

The corrosion resistance of Fe-based amorphous/nanocrystalline coating was attributed to the passive film formed on the surface in NaCl solution, which was composed of Fe and Cr oxides plus fewer Mo and W oxides. The chloride ions decrease the pitting resistance dramatically due to their strong ability to penetrate the passive film, while Mo and W elements will improve the corrosion resistance of amorphous iron alloy by increasing the chemical stability of the passive film and inhibiting pitting corrosion.

Author Contributions: Conceptualization, J.Z. and C.D. (Chunming Deng); Methodology, J.Z. and J.S.; Software, J.Z.; Validation, C.D. (Changguang Deng); Formal Analysis, J.Z.; Investigation, J.Z.; Resources, C.D. (Chunming Deng); Data Curation, C.D. (Chunming Deng) and M.L.; Writing—Original Draft Preparation, J.Z.; Writing—Review and Editing, M.D.; Visualization, J.S.; Supervision, C.D. (Changguang Deng); Project Administration, C.D. (Changguang Deng); Funding Acquisition, C.D. (Changguang Deng).

References

1. Tsutsumi, Y.; Nishikata, A.; Tsuru, T. Pitting corrosion mechanism of Type 304 stainless steel under a droplet of chloride solutions. *Corros. Sci.* **2007**, *49*, 1394–1407. [CrossRef]
2. Pardo, A.; Merino, M.C.; Coy, A.E.; Viejo, F.; Arrabal, R.; Matykina, E. Pitting corrosion behaviour of austenitic stainless steels-combining effects of Mn and Mo additions. *Corros. Sci.* **2008**, *50*, 1796–1806. [CrossRef]
3. Pang, S.J.; Zhang, T.; Asami, K.; Inoue, A. Bulk glassy Fe-Cr-Mo-C-B alloys with high corrosion resistance. *Corros. Sci.* **2002**, *44*, 1847–1856. [CrossRef]
4. Souza, C.A.C.; May, J.E.; Carlos, I.A.; de Oliveira, M.F.; Kuri, S.E.; Kiminami, C.S. Influence of the corrosion on the saturation magnetic density of amorphous and nanocrystalline $Fe_{73}Nb_3Si_{15.5}B_{7.5}Cu_1$ and $Fe_{80}Zr_{3.5}Nb_{3.5}B_{12}Cu_1$ alloys. *J. Non-Cryst. Solids* **2002**, *304*, 210–216. [CrossRef]
5. Cheng, J.B.; Liang, X.B.; Chen, Y.X.; Wang, Z.H.; Xu, B.S. High-temperature erosion resistance of FeBSiNb amorphous coatings deposited by arc spraying for boiler applications. *J. Therm. Spray Technol.* **2013**, *22*, 820–827. [CrossRef]
6. Guo, R.Q.; Zhang, C.; Yang, Y.; Peng, Y.; Liu, L. Corrosion and wear resistance of a Fe-based amorphous coating in underground environment. *Intermetallics* **2012**, *30*, 94–99. [CrossRef]
7. Zhou, H.; Zhang, C.; Wang, W.; Yasir, M.; Liu, L. Microstructure and mechanical properties of Fe-based amorphous composite coatings reinforced by stainless steel powders. *J. Mater. Sci. Technol.* **2015**, *31*, 43–47. [CrossRef]
8. Li, J.; Yang, L.; Ma, H.; Jiang, K.; Chang, C.; Wang, J.-Q.; Song, Z.; Wang, X.; Li, R.-W. Improved corrosion resistance of novel Fe-based amorphous alloys. *Mater. Des.* **2016**, *95*, 225–230. [CrossRef]
9. Liu, L.; Zhang, C. Fe-based amorphous coatings: Structures and properties. *Thin Solid Films* **2014**, *561*, 70–86. [CrossRef]
10. Wang, G.; Huang, Z.; Xiao, P.; Zhu, X. Spraying of Fe-based amorphous coating with high corrosionresistance by HVAF. *J. Manuf. Process.* **2016**, *22*, 34–38. [CrossRef]
11. Wu, H.; Lan, X.; Liu, Y.; Li, F.; Zhang, W.; Chen, Z.; Zai, X.; Zeng, H. Fabrication, tribological and corrosion behaviors of detonation gun sprayed Fe-based metallic glass coating. *Trans. Nonferr. Met. Soc. China* **2016**, *26*, 1629–1637. [CrossRef]
12. Zheng, Z.B.; Zheng, Y.G.; Sun, W.H.; Wang, J.Q. Erosion-corrosion of HVOF-sprayed Fe-based amorphous metallic coating under impingement by a sand-containing NaCl solution. *Corros. Sci.* **2013**, *76*, 337–347. [CrossRef]
13. Zhang, H.; Hu, Y.; Hou, G.; An, Y.; Liu, G. The effect of high-velocity oxy-fuel spraying parameters on microstructure, corrosion and wear resistance of Fe-based metallic glass coatings. *J. Non-Cryst. Solids* **2014**, *406*, 37–44. [CrossRef]
14. Ni, H.S.; Liu, X.H.; Chang, X.C.; Hou, W.L.; Liu, W.; Wang, J.Q. High performance amorphous steel coating prepared by HVOF thermal spraying. *J. Alloy Compd.* **2009**, *467*, 163–167. [CrossRef]
15. Zhou, Z.; Wang, L.; Wang, F.C.; Zhang, H.F.; Liu, Y.B.; Xu, S.H. Formation and corrosion behavior of Fe-based amorphous metallic coatings by HVOF thermal spraying. *Surf. Coat. Technol.* **2009**, *204*, 563–570. [CrossRef]
16. Guo, S.F.; Pan, F.S.; Zhang, H.J.; Zhang, D.F.; Wang, J.F.; Miao, J.; Su, C.; Zhang, C. Fe-based amorphous coating for corrosion protection of magnesiumalloy. *Mater. Des.* **2016**, *108*, 624–631. [CrossRef]
17. Wua, J.; Zhang, S.D.; Sun, W.H.; Gao, Y.; Wang, J.Q. Enhanced corrosion resistance in Fe-based amorphous coatings through eliminating Cr-depleted zones. *Corros. Sci.* **2018**, *136*, 161–173. [CrossRef]
18. Yang, Y.; Zhang, C.; Peng, Y.; Yu, Y.; Liu, L. Effects of crystallization on the corrosion resistance of Fe-based amorphous coatings. *Corros. Sci.* **2012**, *59*, 10–19. [CrossRef]
19. Raicheff, R.; Zaprianova, V.; Gattef, E. Effect of structural relaxation on electrochemical corrosion behaviour of amorphous alloys. *J. Mater. Sci. Lett.* **1997**, *16*, 1701–1704. [CrossRef]
20. Zhang, S.D.; Wu, J.; Qi, W.B.; Wang, J.Q. Effect of porosity defects on the long-term corrosion behaviour of Fe-based amorphous alloy coated mild steel. *Corros. Sci.* **2016**, *110*, 57–70.
21. Long, Z.L.; Chang, C.T.; Ding, Y.H.; Shao, Y.; Zhang, P.; Shen, B.L.; Inoue, A. Corrosion behavior of Fe-based ferromagnetic (Fe, Ni)-B-Si-Nb bulk glassy alloys in aqueous electrolytes. *J. Non-Cryst. Solids* **2008**, *354*, 4609–4613. [CrossRef]
22. Zhang, S.D.; Zhang, W.L.; Wang, S.G.; Gu, X.J.; Wang, J.Q. Characterisation of three-dimensional porosity in an Fe-based amorphous coating and its correlation with corrosion behaviour. *Corros. Sci.* **2015**, *93*, 211–221. [CrossRef]

23. Bakare, M.S.; Voisey, K.T.; Chokethawai, K.; McCartney, D.G. Corrosion behaviour of crystalline and amorphous forms of the glass forming alloy Fe43Cr16Mo16C15B10. *J. Alloys Compd.* **2012**, *527*, 210–218. [CrossRef]

24. Zhang, J.; Liu, M.; Song, J.; Deng, C.; Deng, C. Microstructure and corrosion behavior of Fe-based amorphous coating prepared by HVOF. *J. Alloys Compd.* **2017**, *721*, 506–511. [CrossRef]

25. Zhang, C.; Chan, K.C.; Wu, Y.; Liu, L. Pitting initiation in Fe-based amorphous coatings. *Acta Mater.* **2012**, *60*, 4152–4159. [CrossRef]

26. Naka, M.; Hashimoto, K.; Masumoto, T. High corrosion resistance of amorphous Fe-Mo and Fe-W alloys in HCl. *J. Non-Cryst. Solids* **1978**, *29*, 61–65. [CrossRef]

27. Aghuy, A.A.; Zakeri, M.; Moayed, M.H.; Mazinani, M. Effect of grain size on pitting corrosion of 304L austenitic stainless steel. *Corros. Sci.* **2015**, *94*, 368–376. [CrossRef]

28. Cao, C. On electrochemical techniques for interface inhibitor research. *Corros. Sci.* **1996**, *38*, 2073–2082. [CrossRef]

29. Zhang, J.; Zhang, W.; Yan, C.; Du, K.; Wang, F. Corrosion behaviors of Zn/Al-Mn alloy composite coatings deposited on magnesium alloy AZ31B (Mg-Al-Zn). *Electrochim. Acta* **2009**, *55*, 560–571. [CrossRef]

30. Frankel, G.S. Pitting corrosion of metals: A review of the critical factors. *J. Electrochem. Soc.* **1998**, *145*, 2186–2198. [CrossRef]

31. Malik, A.U.; Kutty, P.C.M.; Siddiqi, N.A.; Andijani, I.N.; Ahmed, S. The influence of pH and chloride concentration on the corrosion behaviour of AISI 316 steel in aqueous solutions. *Corros. Sci.* **1992**, *33*, 1809–1827. [CrossRef]

32. Jinlong, L.; Tongxiang, L.; Chen, W. Surface enriched molybdenum enhancing the corrosion resistance of 316L stainless steel. *Mater. Lett.* **2016**, *171*, 38–41. [CrossRef]

33. Huang, H.-H. Effect of chemical composition on the corrosion behavior of Ni-Cr-Mo dental casting alloys. *J. Biomed. Mater. Res. Banner* **2002**, *60*, 458–465. [CrossRef] [PubMed]

34. Stolica, N. Pitting corrosion on Fe-Cr and Fe-Cr-Ni alloys. *Corros. Sci.* **1969**, *9*, 455–470. [CrossRef]

35. Wang, Y.; Cheng, G.; Wu, W.; Qiao, Q.; Li, Y.; Li, X. Effect of pH and chloride on the micro-mechanism of pitting corrosion for high strength pipeline steel in aerated NaCl solutions. *Appl. Surf. Sci.* **2015**, *349*, 746–756. [CrossRef]

36. Roy, A.K.; Fleming, D.L.; Gordon, S.R. Effect of chloride concentration and pH on pitting corrosion of waste package container materials. In Proceedings of the 190th Meeting of The Electrochemical Society, San Antonio, TX, USA, 6–11 October 1996.

37. Search for the binding energy of an element and line. Available online: http://srdata.nist.gov/xps/ElmSpectralSrch.aspx?selEnergy=PE (accessed on 26 March 2019).

38. Thierry, D.; Zou, F. Localized electrochemical impedance spectroscopy for studying pitting corrosion on stainless steels. *J. Electrochem. Soc.* **1997**, *144*, 1208–1215.

39. Loable, C.; Viçosa, I.N.; Mesquita, T.J.; Mantel, M.; Nogueira, R.P.; Berthom, G.; Chauveau, E.; Roche, V. Synergy between molybdenum and nitrogen on the pitting corrosion and passive film resistance of austenitic stainless steels as a pH-dependent effect. *Mater. Chem. Phys.* **2017**, *186*, 237–245. [CrossRef]

40. Sunseri, C.; Piazza, S.; Quarto, F.D. Photocurrent spectroscopic investigations of passive films on chromium. *J. Electrochem. Soc.* **1990**, *137*, 2411–2417. [CrossRef]

41. Kennedy, J.H.; Frese, K.W. Flatband potentials and donor densities of polycrystalline α-Fe$_2$O$_3$ determined from Mott-Schottky plots. *J. Electrochem. Soc.* **1978**, *125*, 723–726. [CrossRef]

42. Ilevbare, G.O.; Burstein, G.T. The role of alloyed molybdenum in the inhibition of pitting corrosion in stainless steels. *Corros. Sci.* **2001**, *43*, 485–516. [CrossRef]

43. Long, Z.L.; Shao, Y.; Deng, X.H.; Zhang, Z.C.; Jiang, Y.; Zhang, P.; Shen, B.L.; Inoue, A. Cr effects on magnetic and corrosion properties of Fe-Co-Si-B-Nb-Cr bulk glassy alloys with high glass-forming ability. *Intermetallics* **2007**, *15*, 1453–1458. [CrossRef]

44. Streicher, M.A. Development of pitting resistant Fe-Cr-Mo alloys. *Corrosion* **1974**, *30*, 77–91. [CrossRef]

45. Otsubo, F.; Kishitake, K. Corrosion resistance of Fe-16%Cr-30%Mo-(C,B,P) amorphous coatings sprayed by HVOF and APS processes. *Mater. Trans.* **2005**, *46*, 80–83. [CrossRef]